**Energy &
Environmental
Science**

Defect quantification in metal halide perovskites: The solid-state electrochemical alternative

Journal:	*Energy & Environmental Science*
Manuscript ID	EE-COM-05-2021-001525.R1
Article Type:	Communication
Date Submitted by the Author:	13-Jul-2021
Complete List of Authors:	De Keersmaecker, Michel; University of Arizona, Chemical and Environmental Engineering Armstrong, Neal; University of Arizona Optical Sciences Center, Chemistry/Biochemistry/Optical Sciences Ratcliff, Erin; University of Arizona, Departments of Chemical and Environmental Engineering, Chemistry and Biochemistry, Materials Science and Engineering

**SCHOLARONE™
Manuscripts**

COMMUNICATION

Defect quantification in metal halide perovskites: The solid-state electrochemical alternative

Michel De Keersmaecker,[a,b,*] Neal R. Armstrong [b] and Erin L. Ratcliff [a,b,c,*]

Electrochemical methodologies are routinely used to determine energetics and defect density in semiconductor materials under *operando* conditions. For metal halide perovskites, electrochemical methods are restricted to a limited group of non-solvent electrolytes. This challenge is circumvented via a "peel and stick" solid electrolyte that can contain redox active species, is transparent to visible and X-ray photons for simultaneous characterizations, and can be removed for quantification of near-surface composition and energetics using photoelectron spectroscopies. Defects are qualified for both near-stoichiometric and over-stoichiometric $MAPbI_3$ films using controlled hole and electron injection, afforded through potential modulation with respect to a calibrated internal reference. Inclusion of mid-gap redox probes (ferrocene) allows for probing density of states, whereby electron transfer reversibility is shown to be dependent upon the number of ionized defects at the perovskite's band edges. A detailed Coulombic analysis is provided for determination of defect energetics and densities, with a near-stoichiometric film exhibiting a defect density of $\sim 2 \times 10^{17}$ cm^{-3} at 0.1 eV above the valence band. We predict that this easily implemented three-electrode platform will be translatable to *operando* characterization of a range of semiconductor materials, including thin film perovskites, (in)organic semiconductors, quantum dots, and device stacks, where the removable solid electrolyte functions as the "top contact".

Printable metal halide perovskites have demonstrated remarkable advances as active layers in photovoltaics,

[a.] *Department of Chemical and Environmental Engineering, Laboratory for Interface Science of Printable Electronic Materials, The University of Arizona, 1133 E. James E Rogers Way, Tucson, AZ, 85721, USA*

[b.] *Department of Chemistry and Biochemistry, The University of Arizona, 1306 E. University Way, Tucson, AZ, 85721, USA*

[c.] *Department of Materials Science and Engineering, The University of Arizona, 1235 E.James E Rogers Way, Tucson, AZ, 85721, USA*

* corresponding authors.

E-mail: mdekeersmaecker@email.arizona.edu; ratcliff@email.arizona.edu

Phone: +1 (0)520 6265567

Defects are introduced in all semiconductor materials during growth and processing. In general, defects are related to the formation of lattice distortions and impurities, phase transitions, grain boundaries, microstructure, and most importantly, interfaces between active layers and electrical contacts. This highlights the importance of understanding these defects at a fundamental level and the need for more sensitive, selective and *operando* characterization tools as they introduce electronic levels into the bandgap, affecting device performance and stability. Recent developments have demonstrated that the efficiency of light-emitting diodes and photovoltaic cells can be enhanced by simply controlling defect populations. By relying on an easy-to-apply solid-state electrolyte layer in combination with an electrochemical approach that allows the controlled stress modulation to inject holes and electrons in semiconductors, we have the capability to characterize defects and their propagation. This new defect characterization technique could widen the search for novel optoelectronic and photoelectrochemical devices used in energy conversion and storage, along with printable environmental sensors.

photoelectrochemical cells, light emitting diodes, X-ray detectors and biosensors, arising from a decade of research into ink formulations and processing conditions.[1–3] Despite these promising breakthroughs, the complexity of long-term stability continues to limit broad applicability. Characterization of the electronic defects in hybrid organic-inorganic metal halide perovskite materials and interfaces is crucial. While more defect tolerant than conventional semiconductors (ex. GaAs, GaN, etc), printable metal halide perovskite semiconductors exhibit a mixed electronic-ionic conduction mechanism that ultimately contributes to the formation of reactive defects[4,5] at concentrations that limit device performance and long-term stability, which ultimately restricts wide-spread commercialization.[6] For example, ion transport is strongly linked to defect propagation in perovskites, yielding changes to local chemical composition, electronic structure, and physical microstructure.[7–10] All these effects are exacerbated under photon flux, heat, humidity, and/or electrical bias.[11–13] Fundamentally, quantifying these defect concentrations

relative to valence and conduction bands of metal halide perovskites provides critical insights into long-term stability issues in emerging energy conversion technologies. Multiple reports have considered defects, but commonly utilize a space-charge limited current approach; however, in the absence of mobile ions, this often results in misinterpretation and/or misunderstanding of the intrinsic electronic properties of the perovskite. Thus, optimization of opto-electronic properties, and achieving greatly enhanced stabilities necessitates *operando* characterization of correlated chemical-electronic-physical properties at interfaces and in device stacks.

Three-electrode electrochemical measurement techniques have historical precedent for quantification of mid-gap and near valence/conduction band (E_{VB}/E_{CB}) defects in semiconductor materials.[14–17] Inclusion of redox probes facilitates operando mapping of electronic structure, including local density of states, elucidation of surface defect reactivity, and assessment

represent charge injection and charge extraction events in working optoelectronic platforms.[18–20] Additional advantages include sub-parts-per-billion sensitivity for potentiometric and galvanic methods, translation from macro-to nanometer length scales,[21] and direct connections to device performance. Alternatively, electron microscopy, absorption and/or photoelectron spectroscopies techniques have lower sensitivity (parts per thousand), lack operando capabilities, and require multiple techniques to make chemical-electronic-physical connections.[22–25]

Herein we leverage the advantages of (spectro)-electrochemical techniques for defect quantification in metal halide perovskites by using a solvent-free (solid-state) electrolyte, a complement to prior electrochemical characterization of defect chemistry on phase segregation and degradation using non-solvents.[26–30] We circumvent challenges with perovskite solubility via a "stick and peel" solid electrolyte
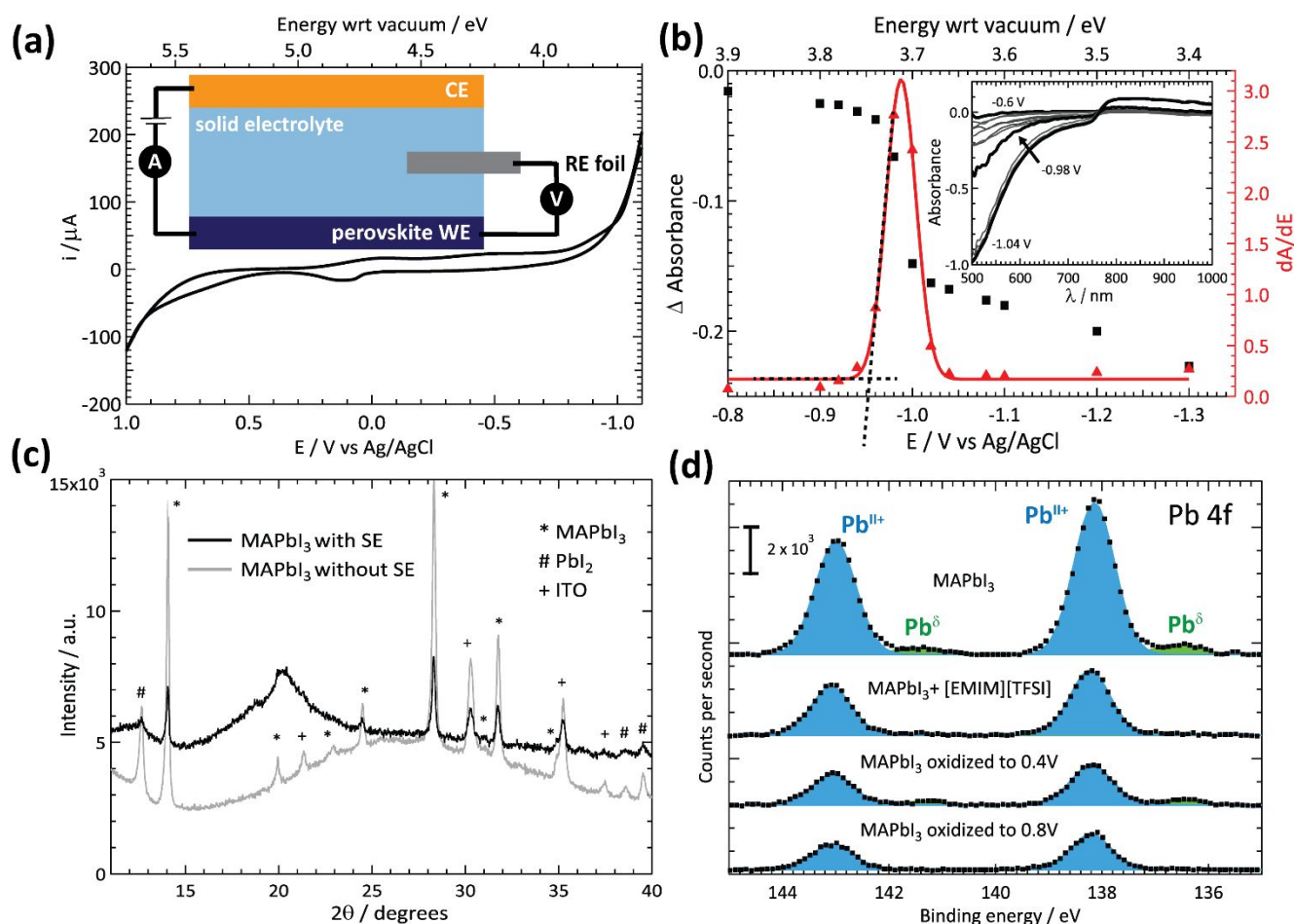
Figure 1: (a) Schematic of the MAPbI₃ half-cell stack structure used for electrochemical characterization. (b) Full band analysis with ■ = A(730 nm) (versus the baseline absorbance A(820 nm)) and ▲ = dA/dE in a potential range of -0.6 V to -0.9 V and -1.1 to -1.3 V with 0.1 increments and -0.9 to -1.1 V with 0.02 V increments, taken from in-situ spectroelectrochemical data for the bleaching of MAPbI₃ conduction band for the stack in (a), with no redox probe, in ambient conditions (inset). The red line is a Gaussian fit with a maximum at 3.72 eV and FWHM of 0.23 ± 0.00(1) eV as a guide for the eye. (c) XRD spectra of MAPbI₃ films with and without a SE top layer; peak assignments for lattice spacings are indicated for MAPbI₃ (*), PbI₂ (#), and ITO (+). (d) High-resolution Pb 4f core level XPS spectra for a clean MAPbI₃ film, a MAPbI₃ film after SE peel, after oxidation to 0.4 V and 0.8 V. Pb^δ is ascribed to under-coordinated lead, where 0≤δ<2.

of defect passivation strategies, as electron transfer events

(SE) that equilibrates electrochemically with the perovskite and

provides optical and X-ray transparency. To demonstrate the power of our technique and the unprecedented stability of these materials during analysis, we focus on methylammonium lead triiodide ($MAPbI_3$), one of the most well-characterized metal halide perovskites. This strategic choice allows for
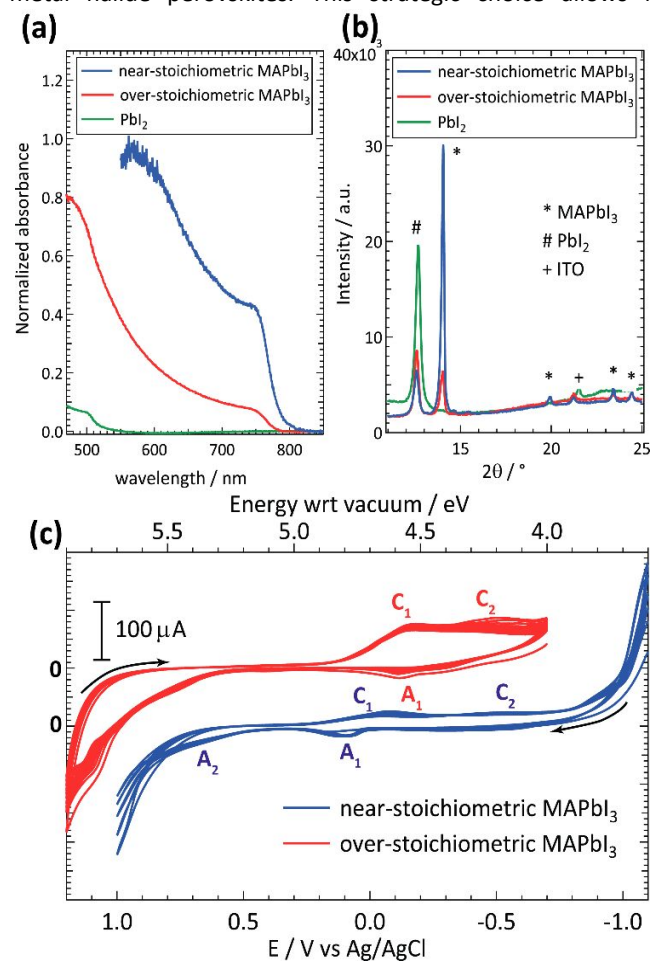
Figure 2: *(a) UV-vis and (b) XRD spectra of PbI_2, over-stoichiometric (excess PbI_2) and near-stoichiometric $MAPbI_3$ films. (c) Five consecutive CVs of an over-stoichiometric (red) and near-stoichiometric (blue) $MAPbI_3$ film in contact with a SE layer without a redox probe in ambient conditions. The red curve is offset by 100 μA for clarity.*

comparison of our observations with several proposed reactivity/degradation mechanisms from experiment and theory, as well as demonstration of reversible and irreversible redox activities.

We note the following key conclusions using our solid-state electrochemical approach. First, we demonstrate the ability to characterize both the valence and conduction band onset using spectroelectrochemistry, with good agreement to photoelectron spectroscopy. This *operando* characterization is compatible with X-ray diffraction and the SE is easily removed for additional surface characterization. We stress that this electrochemical method assesses these states in the presence of mobile carriers and under influence of an electric field. Second, we demonstrate the validity of electrochemistry to detect known decomposition products in metal halide

perovskites, specifically focusing on redox reactions of mobile iodide/triiodide species using over-stoichiometric (excess PbI_2) and near-stoichiometric $MAPbI_3$ films. In short, this approach can assess the quality of printable semiconductor films prior to investing in device optimization. Third, we note that the addition of redox species in the SE allows for electron or hole-collection, thus enabling evaluation of density of states in the presence of device-relevant electric fields[31] as a direct connection to optoelectronic devices and platforms. Fourth, the redox molecule facilitates a significant enhancement in the metal halide perovskite interface stability, as evident in repeated potential cycling and the systematic ability to shift potentials. Fifth, the presence of above valence/below conduction band defects is readily observed, based on the redox probe reversibility, relative to the available states in the conduction or valence band that are accessed. To this last point, a careful, quantitative analysis of charge, as a function of potential, enables determination of defects in a near-stoichiometric film, herein shown to be on the order of 10^{17} cm^{-3} at 0.1 eV above the valence band.

Figure 1 summarizes the capabilities, similar to half-cell configurations of (photo)electrochemical energy conversion and storage platforms,[32,33] that are easily translatable to other semiconductor systems under device-relevant stressors (light bias, heat, ambient gas exposure, etc). In the inset of Figure 1a, the working electrode (WE) is a material stack (i.e. transparent conductive oxide (TCO)/perovskite) interfaced with the SE, comprised of a chemically inert polymer with low oxygen transport (poly(vinylidene fluoride) (PVDF)),[34–36] an ionic liquid for conductivity, and if desired, a redox probe molecule. The reference electrode (RE, Ag/AgCl foil) is imbedded in the SE and sets a reference potential of 0.07 V (versus Fc$^+$/Fc redox couple)[37] and a gold or indium tin oxide (ITO) counter electrode (CE) modulates the electrochemical potential to inject holes or electrons into the perovskite. An in-plane geometry can be adopted for simultaneous UV-vis spectroscopic and X-ray characterization and addition of environmental stress (electric field, humidity, temperature, illumination) is straightforward. Charge selective layers can easily be included between the TCO and perovskite.

In the cyclic voltammogram (CV) in Figure 1a, we observe a low background current in the band gap of the perovskite between 0.7 V vs. Ag/AgCl (5.4 eV vs. surface vacuum) and -0.9 V (3.8 eV). Higher anodic (E > 0.7 V) and cathodic (E < -0.9 V) over-potentials show an exponential increase in current, consistent with charge injection/extraction from valence and conduction bands of $MAPbI_3$.[26,38–40] The sensitivity of the approach is demonstrated in the spectroelectrochemical data in Figure 1b, which shows the change in absorbance with injection of electrons into the conduction band. Typically, resolving energy and density of tail states due to thermal, structural, impurity, and/or compositional disorder has proven challenging for printable electronics.[41] We detect electron injection via bleaching of the band-edge absorbance at 800 nm (inset) as a sigmoidal function of increasing cathodic potentials, consistent with a distribution of states centered at 3.72 eV (and onset at 3.75 eV). A FWHM of 0.23 ± 0.00(1) eV is obtained from the

change in absorbance with potential (dA/dE).[42] Complementary data for hole injection into the valence band is shown in the Supplementary Information section (Figure S1) and agrees with results from ultraviolet photoelectron spectroscopy (Figure S2). The feasibility of operando crystal structure measurements is provided in Figure 1c, which shows X-ray diffraction (XRD) of the MAPbI$_3$ film with and without the SE. Identifiable lattice spacings and detection of common degradation products such as PbI$_2$ are readily observed in over-stoichiometric films.

The integrity of the near surface composition of the perovskite can be probed via X-ray photoelectron spectroscopy (XPS) post removal of the SE, as shown in Figure 1d. Supplemental Note 1 includes additional spectra (Figure S3), fitted parameters (Table S1), elemental ratios (Tables S2-S5), and further discussion. We note that the SE peel-off method could also be used to remove undesired surface defects (top two spectra) or can be used to investigate changes in surface defects when potentials are applied (bottom two spectra).[43] Specifically, the as cast MAPbI$_3$ film shows a small concentration of under-coordinated Pb$^\delta$ ($0 \leq \delta < 2$), which has previously been ascribed to decomposition of PbI$_2$ at the surface, consistent with the detected small fraction of PbI$_2$ in Figure 1c.[44,45] The SE provides a stabilizing effect, where upon removal, defects appear to be removed from the near-surface region, as indicated by the near-stoichiometric Pb/I ratio and removal of aliphatic carbon associated with residual solvent decompositions (Supplemental Note 1).[46] Application of anodic potentials (hole injection processes at 0.4 and 0.8 V) show anion

migration in the perovskite film, discussed further below and in Supplementary Note 1.

In MAPbI$_3$, iodide vacancies are postulated as the primary mobile defects,[47] which is verified by detecting redox-active iodide species in the CV. Figure 2 compares qualitatively over-stoichiometric MAPbI$_3$ (red, excess PbI$_2$). This film exhibits an appreciable concentration of residual PbI$_2$ (absorption band near 500 nm, Figure 2a), relative to a film that is near-stoichiometric MAPbI$_3$ (blue), often used in perovskite solar cells.[48–50] The near-stoichiometric film is evident with a sharp onset in absorption at 800 nm[51] and only trace PbI$_2$ detected by XRD (Figure 2b). Figures 2c and S4 show CVs of the two films. The hydrophobic properties of the PVDF-based copolymer provide a stable perovskite/electrolyte interface, with reproducible current-voltage behavior for five consecutive large potential window scans, even in air. In Figure 2c, a non-Faradaic background current is observed within the bandgap for both films and Faradaic processes are dependent on initial film composition. Table S6 summarizes known electrochemical parameters for labelled peaks (A$_1$/A$_2$ and C$_1$/C$_3$). Peaks A$_1$/C$_1$ correlate with iodide/triiodide (I^-/I_3^-). For the over-stoichiometric film, we observe significantly higher redox activity of I^-/I_3^- [52] and even low intensity ambient light is postulated to catalyze the formation of radical species such as $I_2^{-\bullet}$ (A$_3$: oxidation of I^-; C$_2$: reduction of I_3^-), mitigated through defect sites.
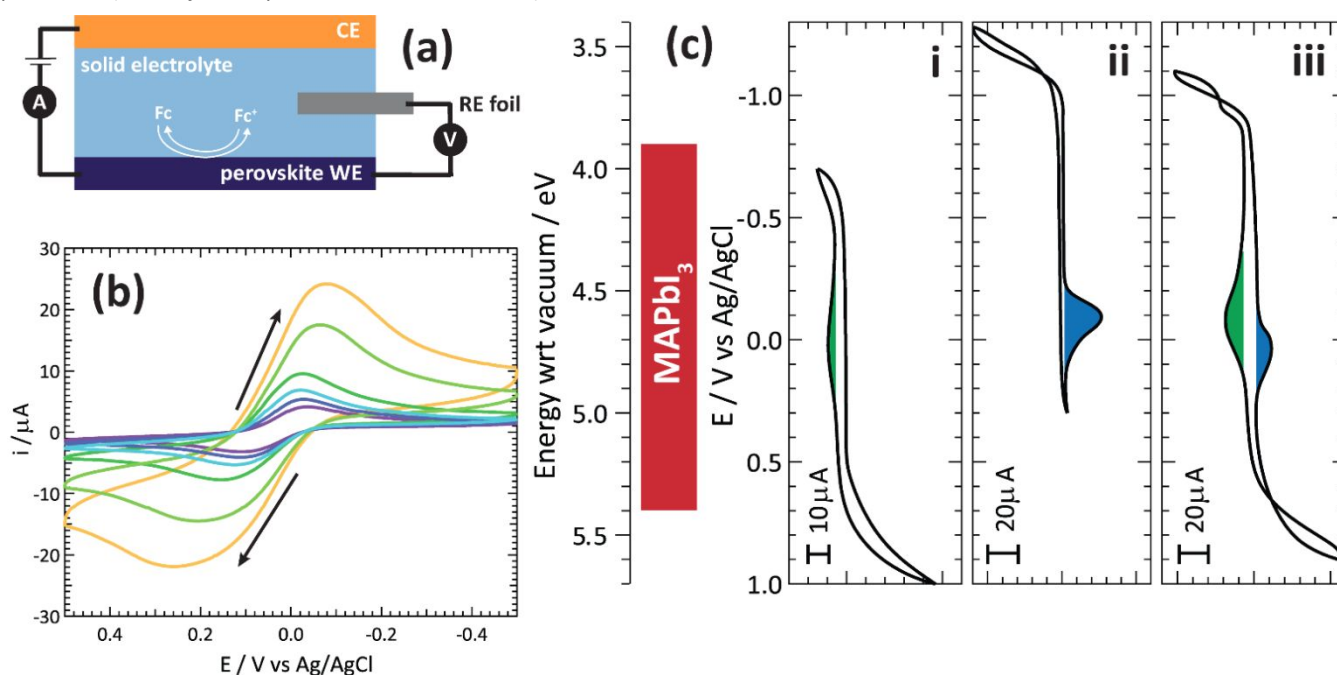
Figure 3: (a) Schematic of the MAPbI$_3$ half-cell stack structure with a 1 mM Fc/Fc$^+$ redox probe in the SE. (b) Scan rate dependent CVs from 0.005 to 0.5 V s^{-1} of Au/SE + Fc/Fc$^+$ stack structure; (c) CVs of MAPbI$_3$/SE + Fc/Fc$^+$ stack in (a) under ambient conditions at a scan rate of 0.05 V s^{-1}. The CV responses are plotted with voltage on y-axis to demonstrate their correspondence to band edge energies for MAPbI$_3$. Experiment includes (i) potential sweep anodic of E_{VB} onset with no electron injection into E_{CB} on cathodic sweep; (ii) potential sweep cathodic of E_{CB} onset with no hole injection into E_{VB} on anodic sweep; and (iii) excursions into both the VB and CB regions. The Fc reduction is highlighted in green, Fc$^+$ oxidation in blue.

migration to the surface to compensate band bending and ion
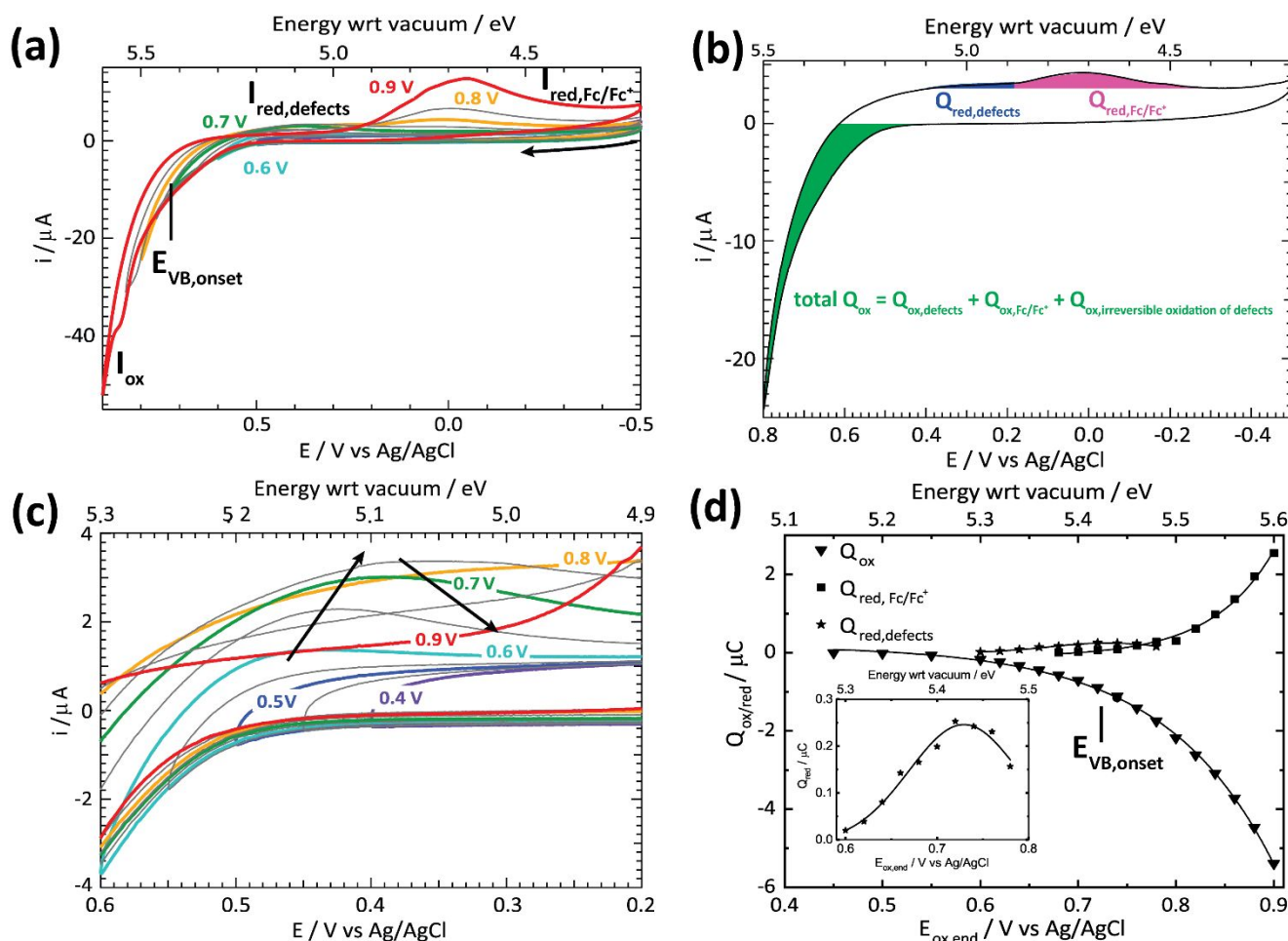
Figure 4: *(a) CVs as a function of anodic potential endpoints approaching and surpassing $E_{VB,onset}$ (0.4 to 0.9 V), followed by cathodic sweep in presence of 1 mM Fc at 0.05 V/s in ambient. Increasingly anodic sweeps yield higher oxidation currents, and on the return sweeps, reduction of "defect states" and reduction of Fc^+ created on the positive sweeps. (b) Integration of the Faradaic oxidation and reduction peaks using cyclic voltammetry. The rest charge is considered non-Faradaic charging at the $MAPbI_3$/electrolyte interface. (c) CVs from (a) that show the defect reduction process in more detail. (d) Charge (Q) integration as a function of $E_{ox,end}$ in (a) separated into (▼) total oxidative charge (Q_{ox}), (*) defect reduction charge ($Q_{red,defects}$), and (■) Fc^+ reduction charge ($Q_{red,Fc/Fc+}$) as described in (b). Inset shows expanded defect reduction region.*

Mid-gap charge transfer in semiconductors is assessed using prototypical redox probes, such as ferrocene/ferrocenium (Fc/Fc⁺). The validity of inclusion of 1 mM Fc in the SE (Figure 3a) and its charge transfer kinetics, diffusivity and stability at a metal (Au) electrode is demonstrated in Figure 3b as a function of scan rate. From peak separation, we determine a heterogeneous rate constant of $k_0 \approx 7 \times 10^{-5}$ cm s⁻¹,[53] with a reductant diffusion coefficient of 1.11×10^{-8} cm² s⁻¹ at 50 mV s⁻¹ in the SE; a diffusion coefficient of 2.65×10^{-7} cm² s⁻¹ was reported in pure [C₄MIM][NTf₂].[54] In Figure 3c, the voltametric reversibility of Fc/Fc⁺ depends on the sweep direction and potential window, based on the number of ionic defects near E_{VB} or E_{CB} (see Figure S5). Briefly, anodic injection of holes at voltages below E_{VB} (E > 5.4 eV; V > 0.7 V) show Fc⁺ reduction (green) on the reverse sweep (panel i) but no clear Fc oxidation peak. Injection of electrons above E_{CB} (E < 3.9 eV; V < -0.8 V) yields Fc oxidation (blue) in the reverse sweep (panel ii) but shows no evident Fc⁺ reduction peak. Reversible, near Nernstian Fc/Fc⁺ behavior is observed when the potential is

systematically modulated between E_{VB} and E_{CB} (panel iii). These results indicate reversible charge transfer can only occur with sufficient overlap between the density of states of redox probe and valence or conduction states (i.e. band bending).

Charge integration, assuming all current above background is Faradaic, allows for defect quantification near E_{VB}. In the interest of brevity, we condense our discussion herein, but refer to Supplemental Note 2 for experimental description, Figure S6a-c for additional data presentation, and Supplemental Note 3 for expanded rationales, assumptions, and step-by-step calculations. Briefly, defect quantification requires an assessment of potential-dependent changes in charge movement across the interface. Defects can be assessed simply by changing the voltage window of each successive CV. In Figure 4a, the oxidative window potentials are systematically increased for anodic potentials, and the current monitored. The data is reproduced in Figures S6 for more clarity and individually considers potential ranges within (a), near (b) and above (c) the valence band. We note that each CV in Figure 4a is a

combination of five full repetitions, indicating no residual hysteresis in the measurement; in other words, electrochemical characterization is not inducing defects. This indicates the stabilizing effect of the use of a redox molecule in the gel electrolyte, relative to without (see Figure S4 for evidence of hysteresis without redox probe for near- and over-stoichiometric films).

In the series of CVs in Figure 4a, there are three important regions of interest: i) anodic current attributed to collective oxidation, where current magnitude exceeds 5 µA at potentials above 0.7 V; ii) cathodic potential steps near 0.5 to 0.2 V, indicate a region of reductive currents on the order of ~ 0.5-3.5 µA (see Figures S6b and S6c); and iii) a reductive wave centered at ~0.0 V associated with Fc^+ reduction (see Figure S6c). These regions are highlighted in Figure 4b using a single cyclic voltammogram for reference, with attributions labelled accordingly. The oxidative wave is attributed to a combination of valence band states, defects and Fc oxidation, with valence band states dominating as we shift more anodic towards E_{VB} (increasing end oxidation potential of linear sweep, $E_{ox,end}$). Interestingly, no Fc^+ reduction is observed until the $E_{VB,onset}$ is surpassed. The reduction region at low $E_{ox,end}$ (< 0.7 V ~ $E_{VB,onset}$) is attributed to defects that are partially reversibly reduced ($Q_{red,defects}$) in the reverse cathodic scan; an expanded region is shown in Figure 4c for clarity.

Following the process outlined in Supplementary Note 3, energy-dependent defect quantification is given in Figure 4d with residuals versus $E_{ox,end}$ in Figure S7. We note the charge distribution for the oxidation process (Q_{ox}, ▼) follows an exponential increase with potential (y = A x exp(-x/t) + y_0 fit is provided), indicative of the distributions expected from Marcus-Gerischer theory for n-type materials at high anodic over-potentials (> 0.8 V), supported by the complementary exponential behavior of Fc^+ reduction (Q_{red},Fc/Fc^+).[14] The shallow surface defects just above E_{VB} (i.e. 5.3 to 5.4 eV) are only partly reduced reversibly ($Q_{red,defects}$, ●), following a Gaussian distribution (inset) with a maximum at 0.729 V (5.429 eV) and a defect density of 2.14 x10^{17} cm^{-3}, as described in Supplementary Note 3. When $E_{ox,end}$ > $E_{VB,onset}$, reduction current associated with the defects decreases, indicating the surface defects could be facilitating Fc^+ reduction (■).

In summary, our easily implemented electrochemical method enables estimations of band edge energies, defect quantification, accessible spectroscopic correlations, and highly sensitive *operando* capabilities for thin film perovskites over a wide potential range. This flexible approach to characterization in semiconductors, using a range of redox couples spanning the bandgap region, with good control over interface stabilities, effective ionic strengths and modulation of local and device-relevant electrical fields, is difficult to implement with any other conventional top contact. In the future, this ground-breaking and flexible technique will enable quantification of defect energies and concentrations on a wide range of (in)organic semiconductor materials, including material blends, where *operando* electrochemical and spectroscopic characterization is critical to design and support next-generation optoelectronic platforms.

Author Contributions

M.D.K. fabricated the test devices and measured the (spectro)electrochemical behavior of different perovskite films both with and without redox probe. E.L.R. originated the concept and assisted in experimental design and data analysis. The manuscript was written with contributions of all authors. All authors have given approval to the final version of the manuscript.

Acknowledgements

Conflicts of interest

There are no conflicts to declare.

Notes and references

1   H. J. Snaith, *Nat. Mater.*, 2018, **17**, 372–376.

2   B. Dou, J. B. Whitaker, K. Bruening, D. T. Moore, L. M. Wheeler, J. Ryter, N. J. Breslin, J. J. Berry, S. M. Garner, F. S. Barnes, S. E. Shaheen, C. J. Tassone, K. Zhu and M. F. A. M. Van Hest, *ACS Energy Lett.*, 2018, **3**, 2558–2565.

3   D. Burkitt, R. Patidar, P. Greenwood, K. Hooper, J. McGettrick, S. Dimitrov, M. Colombo, V. Stoichkov, D. Richards, D. Beynon, M. Davies and T. Watson, *Sustain. Energy Fuels*, 2020, **4**, 3340–3351.

4   A. Zakutayev, C. M. Caskey, A. N. Fioretti, D. S. Ginley, J. Vidal, V. Stevanovic, E. Tea and S. Lany, *J. Phys. Chem. Lett.*, 2014, **5**, 1117–1125.

5   T. Zhang, C. Hu and S. Yang, *Small Methods*, 2020, **4**, 1–20.

6   J. Bisquert and E. J. Juarez-Perez, *J. Phys. Chem. Lett.*, 2019, **10**, 5889–5891.

7   Y. Chen and H. Zhou, *J. Appl. Phys.*, 2020, **128**, 1–18.

8   N. Phung, A. Al-Ashouri, S. Meloni, A. Mattoni, S. Albrecht, E. L. Unger, A. Merdasa and A. Abate, *Adv. Energy Mater.*, 2020, **1903735**, 1–10.

9   S. P. Dunfield, L. Bliss, F. Zhang, J. M. Luther, K. Zhu, M. F. A. M. van Hest, M. O. Reese and J. J. Berry, *Adv. Energy Mater.*, 2020, **10**, 1–35.

10   L. Zhao, R. A. Kerner, Z. Xiao, Y. L. Lin, K. M. Lee, J. Schwartz and B. P. Rand, *ACS Energy Lett.*, 2016, **1**, 595–602.

11   N. G. Park, *Mater. Today*, 2015, **18**, 65–72.

12   C. L. C. Ellis, E. Smith, H. Javaid, G. Berns and D. Venkataraman, *Ion migration in hybrid perovskites*, Elsevier Inc., 2018.

13   C. C. Boyd, R. Cheacharoen, T. Leijtens and M. D. Mcgehee,

Chem. Rev., 2019, **119**, 3418–3451.

14   R. Memming, *Semiconductor Electrochemistry*, WILEY-VCH Verlag GmbH, Weinheim, 2001.

15   H. Gerischer, *J. Phys. Chem.*, 1991, **95**, 1356–1359.

16   N. S. Lewis, *J. Electrochem. Soc.*, 1984, **131**, 2496–2503.

17   A. J. Nozik and R. Memming, *J. Phys. Chem.*, 1996, **100**, 13061–13078.

18   P. A. Kohl and A. J. Bard, *J. Am. Chem. Soc.*, 1977, **99**, 7531–7539.

19   P. A. Kohl and A. J. Bard, *J. Electrochem. Soc.*, 1979, **126**, 59–67.

20   H. Gerischer, *J. Electroanal. Chem.*, 1975, **58**, 263–274.

21   J. Wang, *Talanta*, 2002, **56**, 223–231.

22   Y. Zhou, H. Sternlicht and N. P. Padture, *Joule*, 2019, **3**, 641–661.

23   M. Righetto, S. S. Lim, D. Giovanni, J. Wei and M. Lim, *Nat. Commun.*, 2020, **11**, 1–9.

24   K. X. Steirer, P. Schulz, G. Teeter, V. Stevanovic, M. Yang, K. Zhu and J. J. Berry, *ACS Energy Lett.*, 2016, **1**, 360–366.

25   W. Ming, S. Chen and M. H. Du, *J. Mater. Chem. A*, 2016, **4**, 16975–16981.

26   G. F. Samu, R. A. Scheidt, P. V. Kamat and C. Janáky, *Chem. Mater.*, 2018, **30**, 561–569.

27   G. F. Samu, Á. Balog, F. De Angelis, D. Meggiolaro, P. V. Kamat and C. Janáky, *J. Am. Chem. Soc.*, 2019, **141**, 10812–10820.

28   J. T. Dubose and P. V. Kamat, *J. Am. Chem. Soc.*, 2020, **142**, 5362–5370.

29   H. Iwahara, H. Uchida and K. Morimoto, *J. Electrochem. Soc.*, 1990, **137**, 462–465.

30   H. Uchida, S. Tanaka and H. Iwahara, *J. Appl. Electrochem.*, 1985, **15**, 93–97.

31   A. J. Bandodkar, W. Jia and J. Wang, *Electroanalysis*, 2015, **27**, 562–572.

32   N. Kamaya, K. Homma, Y. Yamakawa, M. Hirayama, R. Kanno, M. Yonemura, T. Kamiyama, Y. Kato, S. Hama, K. Kawamoto and A. Mitsui, *Nat. Mater.*, 2011, **10**, 682–686.

33   J. Janek and W. G. Zeier, *Nat. Energy*, 2016, **1**, 1–4.

34   J. Amici, M. Alidoost, C. Francia, S. Bodoardo, S. Martinez Crespiera, D. Amantia, M. Biasizzo, F. Caldera and F. Trotta, *Chem. Commun.*, 2016, **52**, 13683–13686.

35   P. Bernardo, D. Zampino and G. Clarizia, *Sep. Purif. Technol.*, 2020, **250**, 117201.

36   K. H. Lee, M. S. Kang, S. Zhang, Y. Gu, T. P. Lodge and C. D. Frisbie, *Adv. Mater.*, 2012, **24**, 4457–4462.

37   C. M. Cardona, W. Li, A. E. Kaifer, D. Stockdale and G. C. Bazan, *Adv. Mater.*, 2011, **23**, 2367–2371.

38   J. Even, L. Pedesseau, J. M. Jancu and C. Katan, *J. Phys. Chem. Lett.*, 2013, **4**, 2999–3005.

39   L. Xiong, Y. Guo, J. Wen, H. Liu, G. Yang, P. Qin and G. Fang, *Adv. Funct. Mater.*, 2018, **28**, 1–18.

40   J. Endres, D. A. Egger, M. Kulbak, R. A. Kerner, L. Zhao, S. H. Silver, G. Hodes, B. P. Rand, D. Cahen, L. Kronik and A. Kahn, *J. Phys. Chem. Lett.*, 2016, **7**, 2722–2729.

41   J. F. Wager, *AIP Adv.*, 2017, **7**, 1–10.

42   R. C. Shallcross, Y. Zheng, S. S. Saavedra and N. R. Armstrong, *J. Am. Chem. Soc.*, 2017, **139**, 4866–4878.

43   S. Chen, Y. Liu, X. Xiao, Z. Yu, Y. Deng, X. Dai, Z. Ni and J. Huang, *Joule*, 2020, **4**, 2661–2674.

44   S. Bai, P. Da, C. Li, Z. Wang, Z. Yuan, F. Fu, M. Kawecki, X. Liu, N. Sakai, J. T. W. Wang, S. Huettner, S. Buecheler, M. Fahlman, F. Gao and H. J. Snaith, *Nature*, 2019, **571**, 245–250.

45   Y. H. Lin, N. Sakai, P. Da, J. Wu, H. C. Sansom, A. J. Ramadan, S. Mahesh, J. Liu, R. D. J. Oliver, J. Lim, L. Aspitarte, K. Sharma, P. K. Madhu, A. B. Morales-Vilches, P. K. Nayak, S. Bai, F. Gao, C. R. M. Grovenor, M. B. Johnston, J. G. Labram, J. R. Durrant, J. M. Ball, B. Wenger, B. Stannowski and H. J. Snaith, *Science (80-.).*, 2020, **369**, 96–102.

46   E. J. Juarez-Perez, L. K. Ono, M. Maeda, Y. Jiang, Z. Hawash and Y. Qi, *J. Mater. Chem. A*, 2018, **6**, 9604–9612.

47   S. Tan, I. Yavuz, M. H. Weber, T. Huang, C.-H. Chen, R. Wang, H.-C. Wang, J. H. Ko, S. Nuryyeva, J. Xue, Y. Zhao, K.-H. Wei, J.-W. Lee and Y. Yang, *Joule*, 2020, **4**, 2426–2442.

48   T. J. Jacobsson, J. P. Correa-Baena, E. Halvani Anaraki, B. Philippe, S. D. Stranks, M. E. F. Bouduban, W. Tress, K. Schenk, J. Teuscher, J. E. Moser, H. Rensmo and A. Hagfeldt, *J. Am. Chem. Soc.*, 2016, **138**, 10331–10343.

49   F. Liu, Q. Dong, M. K. Wong, A. B. Djurišić, A. Ng, Z. Ren, Q. Shen, C. Surya, W. K. Chan, J. Wang, A. M. C. Ng, C. Liao, H. Li, K. Shih, C. Wei, H. Su and J. Dai, *Adv. Energy Mater.*, 2016, **6**, 1–9.

50   B. Roose, K. Dey, Y. H. Chiang, R. H. Friend and S. D. Stranks, *J. Phys. Chem. Lett.*, 2020, **11**, 6505–6512.

51   P. Gratia, I. Zimmermann, P. Schouwink, J. H. Yum, J. N. Audinot, K. Sivula, T. Wirtz and M. K. Nazeeruddin, *ACS Energy Lett.*, 2017, **2**, 2686–2693.

52   R. A. Kerner, P. Schulz, J. A. Christians, S. P. Dunfield, B. Dou, L. Zhao, G. Teeter, J. J. Berry and B. P. Rand, *APL Mater.*, 2019, **7**, 1–10.

53   R. S. Nicholson, *Anal. Chem.*, 1965, **37**, 1351–1355.

54   E. I. Rogers, D. S. Silvester, D. L. Poole, L. Aldous, C. Hardacre and R. G. Compton, *J. Phys. Chem. C*, 2008, **112**, 2729–2735.